

Quasi-Continuous Metasurfaces for Orbital Angular Momentum Generation

Menglin L. N. Chen ^{ID}, Member, IEEE, Li Jun Jiang, Fellow, IEEE, and Wei E. I. Sha ^{ID}, Senior Member, IEEE

Abstract—A quasi-continuous composite perfect electric conductor–perfect magnetic conductor metasurface and a systematic metasurface design process are proposed for the orbital angular momentum (OAM) generation. The metasurfaces reflect the incident left circularly polarized (LCP)/right circularly polarized (RCP) plane wave to RCP/LCP vortex beams carrying OAM at normal or oblique direction. Unlike conventional metasurfaces that are composed of discrete scatterers, the scatterers on the proposed metasurface form a quasi-continuous pattern. The patterning of the metasurface is calculated through grating vectors, and no optimization of single scatterer is required. Furthermore, the distortions from local-response discontinuity of discrete scatterers are avoided. This letter provides great convenience to high-quality OAM generation.

Index Terms—Grating vector, orbital angular momentum (OAM), quasi-continuous metasurface.

I. INTRODUCTION

IT IS KNOWN since 1992 that Laguerre–Gaussian modes carry well-defined orbital angular momentum (OAM). Those modes have an azimuthally dependent phase factor, $e^{il\phi}$, where ϕ is the azimuthal angle and l is the OAM index [1]. Since then, OAM has been applied in communications [2], imaging [3], [4], and so on. For example, OAM-based multiplexing and demultiplexing have been implemented at different frequency regimes [5], [6]. As a simple and newly discovered multiplexing approach, OAM multiplexing needs to be studied to overcome the issues of power decay, sensitivity to misalignment, and mode crosstalk for practical applications [7]–[9]. Furthermore, OAM is promising for applications related to the light-matter interaction, such as the manipulation of particles and detection of spinning objects [10], [11].

To introduce OAM to a plane wave, the azimuthal phase factor $e^{il\phi}$ needs to be added along the wave path. Devices for OAM generation include spiral phase plate [12], q-plates [13], gratings [14], metasurfaces [15]–[17], and photonic crystals [18].

Manuscript received December 27, 2018; accepted January 19, 2019. Date of publication January 23, 2019; date of current version March 1, 2019. This work was supported in part by the Research Grants Council of Hong Kong under Grant GRF 17209918, in part by the AOARD under Grant FA2386-17-1-0010, in part by the NSFC under Grant 61271158, in part by the HKU Seed Fund under Grant 201711159228, and in part by the Hundred Talents Program of Zhejiang University under Grant 188020*194231701/208. (Corresponding author: Li Jun Jiang.)

M. L. N. Chen and L. J. Jiang are with the Department of Electrical and Electronic Engineering, The University of Hong Kong, Hong Kong (e-mail: menglin@connect.hku.hk; jianglj@hku.hk).

W. E. I. Sha is with the Key Laboratory of Micro-nano Electronic Devices and Smart Systems of Zhejiang Province, College of Information Science and Electronic Engineering, Zhejiang University, Hangzhou 310027, China (e-mail: weisha@zju.edu.cn).

Digital Object Identifier 10.1109/LAWP.2019.2894772

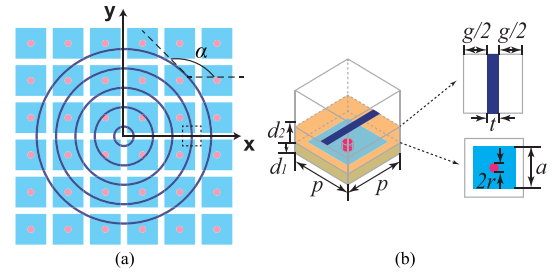


Fig. 1. Schematic pattern of the PEC–PMC metasurface. (a) Top view of the whole metasurface. The inclination angle of the metal strips is denoted by α . (b) Scatterer in the metasurface.

With high flexibility, metasurfaces have been widely used in wave manipulation [19]–[21]. Particularly, as one type of metasurface, geometric-phase-based metasurface changes the local phase of electromagnetic waves by scatterers with varying orientations. This phase modification originates from the change in the polarization state along different paths on the Poincaré sphere [22]. The key point to produce OAM waves by using geometric-phase-based metasurface is to make the local phase change equal to $e^{il\phi}$. Various prototypes of scatterers on these metasurfaces have been proposed for OAM generation, such as split-ring resonators [23], [24] and L-shaped and elliptical nano antennas [25], [26]. However, the performance could be degraded due to the unwanted coupling among scatterers and high-order diffraction. Hence, a lot of efforts need to be taken in the design and optimization of scatterers.

In this letter, we present a quasi-continuous metasurface for OAM generation. The metasurface contains an anisotropic perfect electric conductor (PEC) layer and an isotropic perfect magnetic conductor (PMC) layer. It reflects the incident left circularly polarized (LCP)/right circularly polarized (RCP) plane wave to a RCP/LCP wave, along with a locally modulated geometric phase. The phase distribution on the whole metasurface satisfies $e^{i(l\phi+k_x x+k_y y)}$ so that an OAM of order l can be generated at the k -space position (k_x, k_y) , where k_x and k_y are the transverse wavenumbers. The PEC layer presents a quasi-continuous pattern, and the PMC layer can be realized using any artificial high-impedance surface.

II. METHODOLOGY

Fig. 1(a) illustrates one type of composite PEC–PMC metasurface to produce vortex wave with $l = \pm 2$ [27]. The top PEC layer is composed of concentric metal loops. A mushroom-like high-impedance surface acting as the PMC layer is put beneath

the PEC layer. Any local area on the metasurface can be considered as a PEC scatterer on top of a PMC scatterer. One unit cell is extracted and shown in Fig. 1(b). The geometric and material parameters are the same as in our previous work [27]. The size of one mushroom structure is around $\lambda_0/7$. Therefore, the periodically distributed mushroom can be considered as an isotropic, homogeneous plane. Complex Jones matrix ($J_{xx} J_{xy}; J_{yx} J_{yy}$) is used to model the scatterer. Since it is symmetric about the x - and y -axes, we have $J_{xy} = J_{yx} = 0$. The metal-strip array behaves like a parallel-plate waveguide. The cutoff frequency of corresponding TE₁ mode is $1/(2g\sqrt{\mu\epsilon})$, where g is the gap between adjacent metal strips [28]. Below the cutoff frequency, the y -polarized component will be totally reflected with a π phase shift ($J_{yy} = -1$). The penetrated x -polarized component will be reflected by the PMC plane without phase shift ($J_{xx} = 1$). When the composite structure is illuminated by a circularly polarized wave, the polarization state will be changed from left to right and vice versa. It should be noticed that the whole metasurface is composed of those scatterers with different orientations. Therefore, besides the polarization flip, the reflected wave is accompanied by an additional phase that is equal to $e^{\pm 2i\alpha}$, where α is the inclination angle between the metal-strip tangent and x -axis. The plus/minus sign is taken when the incident wave is LCP/RCP. As can be read from the figure, $\alpha = \phi + \pi/2$. Thus, the reflected wave carries an OAM of order ± 2 . Usually, for geometric-phase-based metasurfaces, rotation of the discrete scatterers breaks the periodicity along the x - and y -directions, resulting in the undesired mutual coupling between the nearest-neighbor scatterers. However, in the composite PEC–PMC metasurface, individual control of the two orthogonal polarizations is realized by the PEC and PMC layers, respectively. No rotation operation is required for the scatterers on the PMC layer. Meanwhile, induced current is continuously guided along the smoothly connected metal strips on the PEC layer. From this point of view, compared to the discrete geometric-phase-based scatterers, the unwanted mutual coupling among the PEC–PMC scatterers is significantly reduced. Moreover, by keeping the local period small enough, no high-order diffraction exists.

Regarding vortex beams carrying arbitrary orders of OAM, in conventional metasurfaces, discrete scatterers are placed at specific locations with predesigned orientations [23]–[26]. However, the discontinuity and aperiodicity induced by the discrete scatterers will distort the near-field pattern [27] and lower the efficiency. To achieve a continuous phase shift on the metasurface, the discrete scatterers should be continuously and smoothly connected. For practical implementation, we consider the metal strips as a grating and model them using grating vectors. An arbitrary metal-strip pattern is drawn in Fig. 2. The grating vector is perpendicular to the tangent of metal strips. In other words, the grating vector is the normal vector of the curve of the metal strips. In polar coordinates, it is written as

$$\begin{aligned} \mathbf{K}_g(r, \phi) &= K_r \hat{\mathbf{r}} + K_\phi \hat{\mathbf{\phi}} \\ &= K_0(r, \phi) \cos[\theta(r, \phi) - \phi] \hat{\mathbf{r}} \\ &\quad + K_0(r, \phi) \sin[\theta(r, \phi) - \phi] \hat{\mathbf{\phi}} \end{aligned} \quad (1)$$

where $K_0(r, \phi)$ is the local spatial frequency at (r, ϕ) .

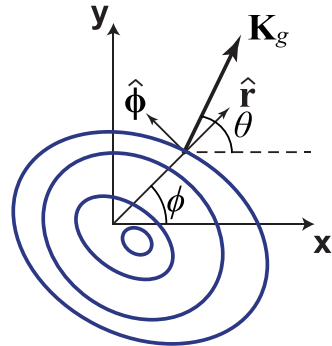


Fig. 2. Arbitrary metal-strip pattern modeled by the grating vector \mathbf{K}_g which is normal to the tangent of the metal strips.

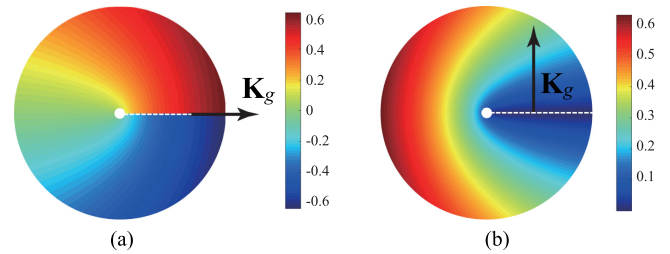


Fig. 3. Calculated g when (a) $m = 0.5$, $a = b = 0$, $D = 0$, $A = 1$ and (b) $m = 0.5$, $a = b = 0$, $D = \pi/2$, $A = 1$.

As discussed, the orientation of the local metal segments characterized by θ determines the geometric phase, which will contribute to the phase shift for the wave manipulation. To produce vortex beams radiating at the desired direction, θ should satisfy

$$\theta(r, \phi) = m\phi + ar \cos \phi + br \sin \phi + D \quad (2)$$

where $m = l/2$ and is also called the topological charge of the structure. The second and third terms in $\theta(r, \phi)$ are introduced for realizing oblique reflection. $a = k_x/2$, $b = k_y/2$. D is a phase constant that determines the direction of \mathbf{K}_g at the origin.

To ensure the continuity of the grating, it is required that $\nabla \times \mathbf{K}_g = 0$ [29]. By substituting (2) into (1), the general solution of K_0 fulfilling the zero divergence condition is of the form

$$K_0 = A \frac{e^{ar \sin \phi - br \cos \phi}}{r^m} \quad (3)$$

where A is a scaling factor.

It is supposed that the closed metal strip could be mathematically described by a curve equation $g(r, \phi) = C$. ∇g is the normal vector of the curve. Therefore, $\nabla g = \mathbf{K}_g$, and it is solved by integrating \mathbf{K}_g over an arbitrary path

$$g(r, \phi) = \int_{(r_0, \phi_0)}^{(r, \phi)} K_r dr + \int_{(r, \phi_0)}^{(r, \phi)} r K_\phi d\phi. \quad (4)$$

In Fig. 3, we show the calculated g when $\theta(r, \phi) = m\phi + D$. As expected, the orientation of the contour line coincides with $\theta(r, \phi)$. The grating vector is perpendicular to the contour line, and its initial orientation at $\phi = 0$ is determined by D , which is horizontal when $D = 0$ and vertical when $D = \pi/2$.

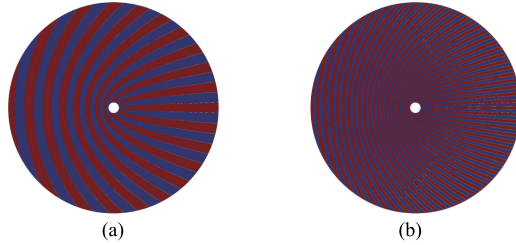


Fig. 4. Binary grating generated from the calculated g in Fig. 3(b) when the scaling factor (a) $A = 100$ and (b) $A = 300$.

A Lee-type binary grating is then generated from g [30]. Fig. 4 shows two gratings with different scaling factors A . The grating is a desired pattern for the PEC layer. The local orientations of the two patterns are identical, while the local periods are different. Since adjacent metal strips function as a parallel-plate waveguide, proper value of A needs to be chosen so that their gap is small enough to guarantee that the operating frequency is far below the cutoff frequency of the TE_1 mode.

III. SIMULATION

For the PEC layer in Fig. 4(b), the outer radius of the pattern is 100 mm, and the inner radius is 5 mm. Two scenarios are compared in which the ideal PMC boundary and the mushroom-like high-impedance surface are applied beneath the PEC layer, respectively. Simulations are done in CST MWS. The metasurface is illuminated by an LCP Gaussian wave with the beam waist of 50 mm at 6.2 GHz. Fig. 5 shows the amplitude and phase distributions of the reflected RCP field component at a transverse plane 20 mm away from the metasurface. We see the field distribution of an OAM wave with $l = 1$. A clear phase singularity is observed. The phase encounters a total 2π change along a closed path enclosing the center. The simulated fields in the two scenarios show a good agreement with each other.

The efficiency of the unit cell can be used to evaluate the performance of the design. The parameters for the mushroom-like high-impedance surface remain the same for all metasurfaces. Hence, we can assume $J_{xx} = 1$ all the time. The y -polarized component will be totally reflected due to presence of the ground plane. However, the reflection phase depends on the gap between the metal strips. Here, we write $J_{yy} = e^{ip}$. For the incidence of a circularly polarized wave, incident components are $i_x = 1$, $i_y = \pm i$. The reflected wave components $r_x = J_{xx} = 1$, $r_y = \pm i J_{yy} = \pm ie^{ip}$. The amplitude of the converted cross-circularly polarized component is $a = (r_x \pm ir_y)/\sqrt{2} = (1 - e^{ip})/\sqrt{2}$. The efficiency of the unit cell, which is equal to the ratio of the power of the converted wave to that of the incident wave, is $|1 - e^{ip}|^2/4$. Clearly, for the ideal case that $p = \pi$, the efficiency is 1. The metasurface shown in Fig. 1 has been demonstrated to exhibit nearly perfect efficiency [27]. For the metasurface with nonuniformly distributed metal strips, we calculate the efficiency using the power of the reflected RCP wave divided by that of the incident wave. The efficiency of the metasurface for Fig. 5 is 94%. The far-field radiation patterns of both the copolar-

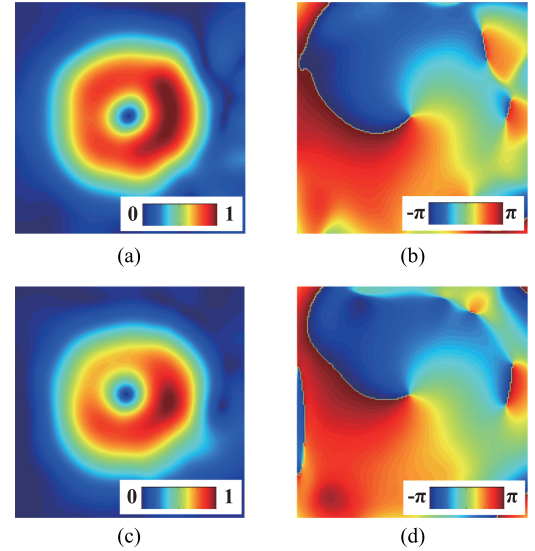


Fig. 5. Simulated field distributions at a transverse plane 20 mm away from the metasurface with $m = 0.5$. (a) Amplitude and (b) phase of the field when the metal strips are placed on an ideal PMC boundary. (c) Amplitude and (d) phase of the field when the metal strips are placed on the mushroom-like high-impedance surface.

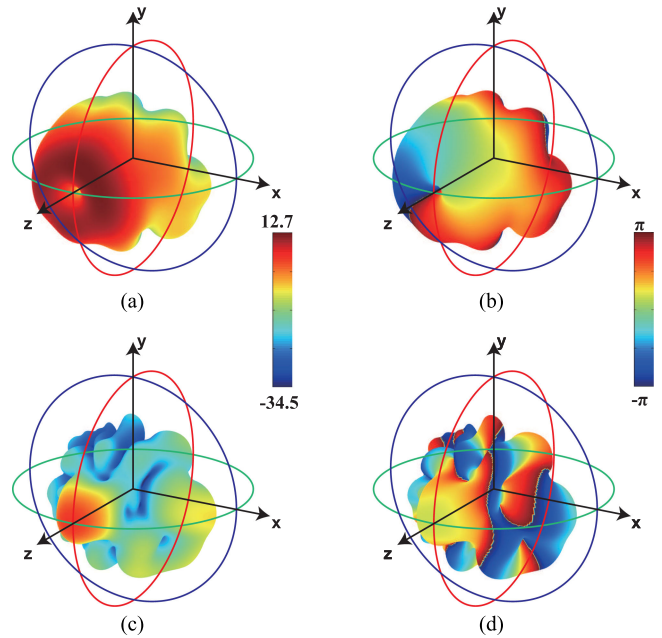


Fig. 6. Simulated far-field radiation patterns for the metasurface with $m = 0.5$. (a) Directivity and (b) phase of the cross-polarized (RCP) component; (c) directivity and (d) phase of the copolarized (LCP) component.

ized component and cross-polarized component are plotted in Fig. 6. The maximum directivity for the RCP component is 12.7 dBi and it is only 5.5 dBi for the LCP component. Moreover, the directivity for the converted component presents a donut shape with a gradual phase change around the vortex axis, while the copolarized component does not show such feature.

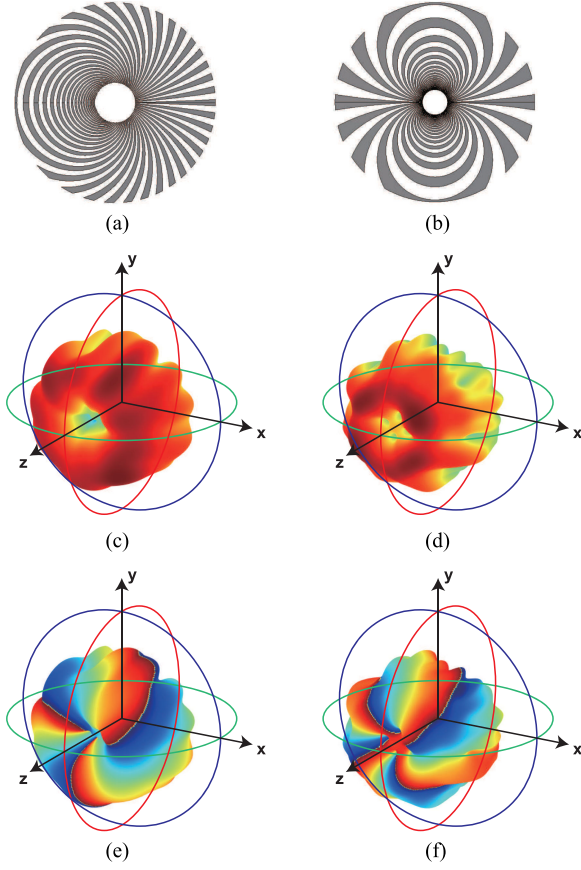


Fig. 7. Quasi-continuous PEC–PMC metasurfaces to produce OAM at normal direction and their far-field radiation patterns. When $m = 1.5$, (a) the top view of the PEC layer, (c) directivity, and (e) phase of the RCP component. When $m = 2$, (b) the top view of the PEC layer, (d) directivity, and (f) phase of the RCP component.

In following simulations, we will use the ideal PMC boundary for simplicity. Metasurfaces for generating OAM with other orders can be built based on the same procedure. The top metal-strip layers with the topological charge $m = 1.5$ and $m = 2$ are shown in Fig. 7. The far-field directivity and phase patterns indicate the successful generation of OAM with order $l = 3$ and $l = 4$.

Regarding oblique reflection to be manipulated, transverse wavenumbers k_x and k_y need to be introduced. They are calculated based on the desired reflected wave direction (θ_0, ϕ_0) as follows:

$$k_x = k_0 \cos \phi_0 \sin \theta_0 \quad k_y = k_0 \sin \phi_0 \sin \theta_0. \quad (5)$$

Then, the required orientation $\theta(r, \phi)$ of metal strips is found from (2). By following the calculations in (3) and (4), the pattern of the PEC layer can be generated. Fig. 8 displays the reflected OAM waves at different directions. As expected, the OAM indexes are 1 in Fig. 8(a) and 3 in Fig. 8(b). The simulated directivity is consistent with our objective. It is worth noting that the proposed design is not limited to radio regime, as long as the responses of the PMC and PEC layers are replicated. For example, in terahertz regime, graphene-based high-impedance surfaces [31] and dielectric metasurfaces [32] can be used as

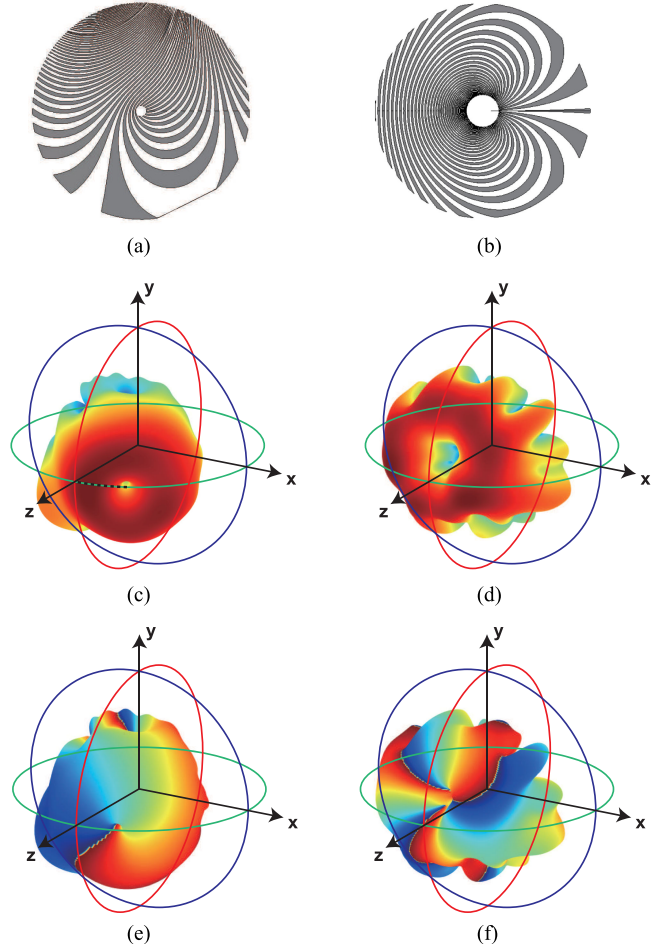


Fig. 8. Quasi-continuous PEC–PMC metasurfaces to produce OAM at oblique directions and their far-field radiation patterns. When $m = 0.5$, $\theta_0 = 20^\circ$, $\phi_0 = 0$, (a) the top view of the PEC layer, (c) directivity, and (e) phase of the RCP component. When $m = 1.5$, $\theta_0 = 10^\circ$, $\phi_0 = 90^\circ$, (b) the top view of the PEC layer, (d) directivity, and (f) phase of the RCP component.

magnetic mirrors. In optical regime, dielectric metamaterials acting as perfect reflectors with the reflection phases of π and zero could be applied [33].

IV. CONCLUSION

We have proposed a quasi-continuous PEC–PMC metasurface with a systematic design route to generate vortex beams at normal and oblique directions. The introduction of spatial phase to the incident plane wave is based on the concept of geometric phase. Specifically, the local phase shift depends on the orientation of the metal strips of the PEC layer. Patterning of the metal strips is accomplished with the assistance of grating vector, which offers a simple and effective way to design the whole metasurface. Different from existing design protocols for geometric-phase-based metasurfaces, complicated optimization process of single scatterer is not needed. Furthermore, thanks to the quasi-continuous geometries, high-order diffraction from discrete scatterers is avoided.

REFERENCES

- [1] L. Allen, M. W. Beijersbergen, R. J. C. Spreeuw, and J. P. Woerdman, “Orbital angular momentum of light and the transformation of Laguerre-Gaussian laser modes,” *Phys. Rev. A*, vol. 45, pp. 8185–8189, 1992.
- [2] A. E. Willner *et al.*, “Optical communications using orbital angular momentum beams,” *Adv. Opt. Photon.*, vol. 7, pp. 66–106, 2015.
- [3] F. Tamburini, G. Anzolin, G. Umbriaco, A. Bianchini, and C. Barbieri, “Overcoming the Rayleigh criterion limit with optical vortices,” *Phys. Rev. Lett.*, vol. 97, 2006, Art. no. 163903.
- [4] K. Liu, Y. Q. Cheng, Z. C. Yang, H. Q. Wang, Y. L. Qin, and X. Li, “Orbital-angular-momentum-based electromagnetic vortex imaging,” *IEEE Antennas Wireless Propag. Lett.*, vol. 14, pp. 711–714, 2015.
- [5] F. Tamburini, E. Mari, A. Sponselli, B. Thidé, A. Bianchini, and F. Romanato, “Encoding many channels on the same frequency through radio vorticity: First experimental test,” *New J. Phys.*, vol. 14, 2012, Art. no. 033001.
- [6] Y. Yan *et al.*, “High-capacity millimetre-wave communications with orbital angular momentum multiplexing,” *Nature Commun.*, vol. 5, 2014, Art. no. 4876.
- [7] G. D. Xie *et al.*, “Performance metrics and design considerations for a free-space optical orbital-angular-momentum multiplexed communication link,” *Optica*, vol. 2, pp. 357–365, 2015.
- [8] N. B. Zhao, X. Y. Li, G. F. Liu, and J. M. Kahn, “Capacity limits of spatially multiplexed free-space communication,” *Nat. Photonics*, vol. 9, pp. 822–826, 2015.
- [9] R. Gaffoglio, A. Cagliero, G. Vecchi, and F. P. Andriulli, “Vortex waves and channel capacity: hopes and reality,” *IEEE Access*, vol. 6, pp. 19814–19822, 2018.
- [10] D. G. Grier, “A revolution in optical manipulation,” *Nature*, vol. 424, pp. 21–27, 2003.
- [11] M. P. J. Lavery, F. C. Speirsits, S. M. Barnett, and M. J. Padgett, “Detection of a spinning object using lights orbital angular momentum,” *Science*, vol. 341, pp. 537–540, 2013.
- [12] M. Beijersbergen, R. Coerwinkel, M. Kristensen, and J. Woerdman, “Helical-wavefront laser beams produced with a spiral phaseplate,” *Opt. Commun.*, vol. 112, pp. 321–327, 1994.
- [13] L. Marrucci, C. Manzo, and D. Paparo, “Optical spin-to-orbital angular momentum conversion in inhomogeneous anisotropic media,” *Phys. Rev. Lett.*, vol. 96, 2006, Art. no. 163905.
- [14] K. Huang *et al.*, “Spiniform phase-encoded metagratings entangling arbitrary rational-order orbital angular momentum,” *Light, Sci. Appl.*, vol. 7, p. 17156, 2018, Art. no. 17156.
- [15] J. Yang *et al.*, “Generation of radio vortex beams with designable polarization using anisotropic frequency selective surface,” *Appl. Phys. Lett.*, vol. 112, 2018, Art. no. 203501.
- [16] S. X. Yu, L. Li, G. M. Shi, C. Zhu, and Y. Shi, “Generating multiple orbital angular momentum vortex beams using a metasurface in radio frequency domain,” *Appl. Phys. Lett.*, vol. 108, 2016, Art. no. 241901.
- [17] H. Y. Shi *et al.*, “Transparent metasurface for generating microwave vortex beams with cross-polarization conversion,” *Materials*, vol. 11, 2018, Art. no. 2448.
- [18] M. L. N. Chen, L. J. Jiang, and W. E. I. Sha, “Generation of orbital angular momentum by a point defect in photonic crystals,” *Phys. Rev. Appl.*, vol. 10, 2018, Art. no. 014034.
- [19] T. J. Cui, M. Q. Qi, X. Wan, J. Zhao, and Q. Cheng, “Coding metamaterials, digital metamaterials and programmable metamaterials,” *Light, Sci. Appl.*, vol. 3, 2014, Art. no. e218.
- [20] M. L. N. Chen, L. J. Jiang, and W. E. I. Sha, “Detection of orbital angular momentum with metasurface at microwave band,” *IEEE Antennas Wireless Propag. Lett.*, vol. 17, no. 1, pp. 110–113, Jan. 2018.
- [21] H. Y. Shi *et al.*, “Generation of multiple modes microwave vortex beams using active metasurface,” *IEEE Antennas Wireless Propag. Lett.*, vol. 18, no. 1, pp. 59–63, Jan. 2019.
- [22] M. V. Berry, “The adiabatic phase and Pancharatnam’s phase for polarized light,” *J. Modern Opt.*, vol. 34, no. 11, pp. 1401–1407, 1987.
- [23] M. L. N. Chen, L. J. Jiang, and W. E. I. Sha, “Ultrathin complementary metasurface for orbital angular momentum generation at microwave frequencies,” *IEEE Trans. Antennas Propag.*, vol. 65, no. 1, pp. 396–400, Jan. 2017.
- [24] M. L. N. Chen, L. J. Jiang, and W. E. I. Sha, “Orbital angular momentum generation and detection by geometric-phase based metasurfaces,” *Appl. Sci.*, vol. 8, 2018, Art. no. 362.
- [25] E. Karimi, S. A. Schulz, I. De Leon, H. Qassim, J. Upham, and R. W. Boyd, “Generating optical orbital angular momentum at visible wavelengths using a plasmonic metasurface,” *Light, Sci. Appl.*, vol. 3, no. 5, 2014, Art. no. e167.
- [26] X. L. Ma *et al.*, “A planar chiral meta-surface for optical vortex generation and focusing,” *Sci. Rep.*, vol. 5, 2015, Art. no. 10365.
- [27] M. L. N. Chen, L. J. Jiang, and W. E. I. Sha, “Artificial perfect electric conductor-perfect magnetic conductor anisotropic metasurface for generating orbital angular momentum of microwave with nearly perfect conversion efficiency,” *J. Appl. Phys.*, vol. 119, no. 6, 2016, Art. no. 064506.
- [28] D. M. Pozar, *Microwave Engineering*. Hoboken, NJ, USA: Wiley, 2009.
- [29] A. Niv, G. Biener, V. Kleiner, and E. Hasman, “Formation of linearly polarized light with axial symmetry by use of space-variant subwavelength gratings,” *Opt. Lett.*, vol. 28, no. 7, pp. 510–512, 2003.
- [30] W. H. Lee, “Binary synthetic holograms,” *Appl. Opt.*, vol. 13, no. 7, pp. 1677–1682, 1974.
- [31] X. C. Wang, W. S. Zhao, J. Hu, and W. Y. Yin, “Reconfigurable terahertz leaky-wave antenna using graphene-based high-impedance surface,” *IEEE Trans. Nanotechnol.*, vol. 14, no. 1, pp. 62–39, Jan. 2015.
- [32] Z. J. Ma *et al.*, “Terahertz all-dielectric magnetic mirror metasurfaces,” *ACS Photon.*, vol. 3, pp. 1010–1018, 2016.
- [33] P. Moitra *et al.*, “Large-scale all-dielectric metamaterial perfect reflectors,” *ACS Photon.*, vol. 2, pp. 692–698, 2015.